



Dual-Ion NiNc Battery: A Sustainable Revolution for Sodium Organic Batteries

Jinkwang Hwang,^{*[a]} Kazuhiko Matsumoto,^[a] Rika Hagiwara,^[a] Shusaku Ukai,^[b] Hiroshi Shinokubo,^[b] and Ji-Young Shin^{*[b]}

Dual-ion mobilities of Na organic batteries are investigated with in-situ XRD analysis and computational estimation considering molecular alignments in the solid state, signifying the interactive variations of ionic-pairs of an ionic liquid electrolyte and an antiaromatic molecule, nickel(II) norcorrole (NiNc). An appropriate cavity sphere in three-dimensional molecular align-

ments dispensed mobilities of dual-ion in an ionic liquid, resulting in high battery capacities, supplemented with the comparison of Mes-NiNc and Ph-NiNc molecular alignments. In-situ XRD experiment, computation, and simulation perspectives afforded prospective insertion and desertion behaviors of cations and anions.

1. Introduction

Sodium-ion batteries have been significantly attractive to scientists and engineers in energy-related science and engineering fields because of the sizeable natural abundance with low cost for sodium.^[1] Similar chemical properties of Na and Li have been facilitated to afford proficient battery electrode materials, whose achievements have been primarily in suitable inorganic materials: Most cases have been derivative in the use of oxides and polyanionic compounds.^[2] However, a larger atomic mass and ionic radius of Na^+ than that of Li^+ has been the primary factor in having low energy density and charge/discharge performances. The recent desire to accomplish outstanding rechargeable batteries is likely to be obtained using organic compounds for electrode materials, manipulating sustainability and producibility of charge and discharge processes.^[3] Through the previous research, we have reported excellent Li^+ and Na^+ collaborative metal-organic batteries afforded with organic electrodes of an antiaromatic molecule, nickel(II) norcorrole (NiNc).^[4] We have comprehended that the critical factor awarding efficient battery performances is antiaromaticity. Nevertheless, exploring other prospective factors is necessary, kept track of, and the related investigation is reported herein.

The accomplishment of excellent organic batteries has been attempted with distinct approaches to mitigate organic electrode dissolution.^[3,4] Metal-organic frameworks (MOFs),

holding rigid and homogeneous porosity, super-ionic sieving capabilities were adopted as a capable artificial separator to build healthier rechargeable organic batteries in K. Kang's research. The system has been introduced as perm-selective MOF gel membrane integrity.^[5]

In early reports, NiNc, described as a stable antiaromatic porphyrinoid, has been introduced to exhibit unique alignments of the molecules in both solid and solution states, substantially related to dynamics of magnetic properties.^[6] Molecular stackings of the antiaromatic compounds derived the enhancement of aromatic character, depending on the meso-substituents.^[6c] A uniquely staked, triple-decker structure of phenyl-substituted NiNc (Ph-NiNc) was elucidated in the crystallographic data. In contrast, the crystal structure of mesityl-substituted NiNc (Mes-NiNc) revealed the prohibition of molecular stackings in the crystalline. Such packing structures in crystalline states are noteworthy to afford the practical permeability of electrolytic ions to manipulate the post's high durability. The conducting factor of stable antiaromatic molecules towards the active battery-electrode materials is substantial for efficient charge-and-discharge performances.

McCullough et al. and Carlin et al. have first proposed the dual-ion battery with both cation and anion intercalating mobiles.^[7] A highly concentrated ionic liquid electrolyte (50 mol% $\text{Na}[\text{FSA}]-[\text{C}_2\text{C}_1\text{im}][\text{FSA}]$ ($[\text{C}_2\text{C}_1\text{im}]^+$: 1-ethyl-3-methylimidazolium and $[\text{FSA}]^-$: bis(fluorosulfonyl)amide)^[8] has been introduced in our rechargeable organic batteries, whose system occupied nickel norcorrole (NiNc) as an active electrode material in sodium-organic batteries. Outcomes of the batteries were excellent, exhibiting inherent charge-discharge behaviors with high discharge capacity, high stability, and high Coulombic efficiency.^[4c] We demonstrated the excellent redox durability in the mechanism of a dual-ion battery of $[\text{FSA}]^-$ and Na^+ , whose further investigation is necessary to verify the hypothesis.

Comparison research to validate the interconnection and inter-relationship between the characteristic antiaromaticity and the permeability of 3D hierarchical packings in the

[a] Prof. J. Hwang, Prof. K. Matsumoto, Prof. R. Hagiwara
Fundamental Energy Science Department
Graduate School of Energy Science, Kyoto University
Kyoto, 606-8501, Japan
E-mail: hwang.jinkwang.5c@kyoto-u.ac.jp

[b] S. Ukai, Prof. H. Shinokubo, Prof. J.-Y. Shin
Department of Molecular and Macromolecular Chemistry
Graduate School of Engineering, Nagoya University
Nagoya, 464-8603, Japan
E-mail: jyshin@chembio.nagoya-u.ac.jp

 Supporting information for this article is available on the WWW under
<https://doi.org/10.1002/batt.202100193>

electrode materials can signify the importance of scattering capability of ionic components in the battery electrolytes and high structural stability of the electrode materials during the charge/discharge processes. Herein, we report the investigations of battery behaviors of Na-NiNc batteries in complementing them with two different active electrode materials, Ph-NiNc having meso-phenyl groups and Mes-NiNc having meso-mesityl groups. We attempted to comprehend how different three-dimensional alignments associate with the battery capacities upon the examination.

2. Results and Discussion

The synthetic procedure of Ph-NiNc and Mes-NiNc (Figure 1) have followed the literature methods as previously published.^[6] Their packing diagrams with space-filling models are based on

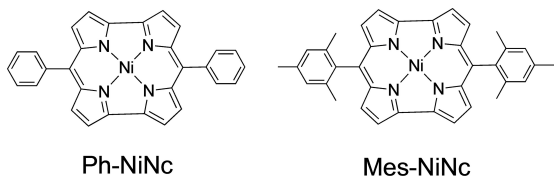


Figure 1. Molecular structures of Ph-NiNc and Mes-NiNc.

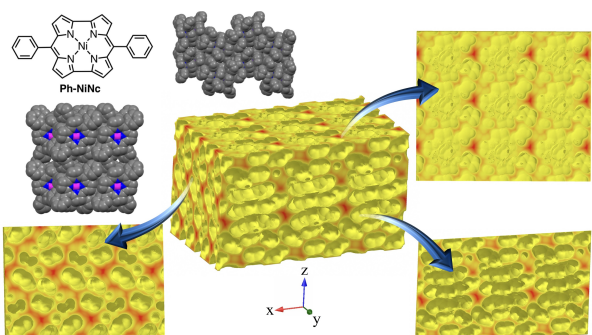


Figure 2. Molecular packing patterns of Ph-NiNc, represented with space filling model, and the display of the void spaces.

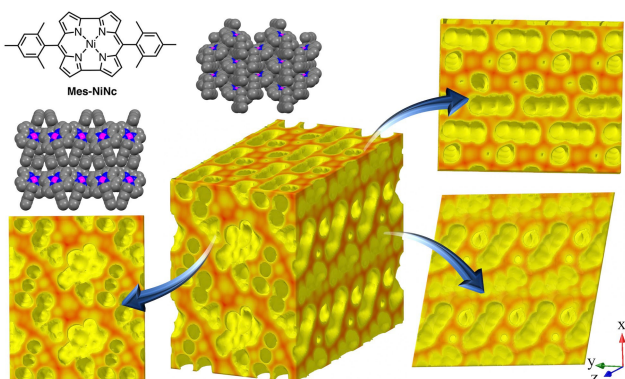


Figure 3. Molecular packing patterns of Mes-NiNc, represented with space filling model, and the display of the void spaces.

single crystal crystallographic data. The packing structure of Ph-NiNc presented a significantly tightened alignment pattern (Figure 2), while that of Mes-NiNc provided a loose packing pattern (Figure 3). Vacant spaces in the crystalline states were simulated for tracking the positions of dual-ion insertion/desertion during charge-discharge processes. The simulation came up with sponge-like displays for the occupancy and the vacancy in a complementary way: The hollowed space has been filled with the NiNc molecules. Accordingly, the occupied space with either yellow or red can be the actual vacancy that is probable for electrolyte ions. The red-colored spots represent the high permeable positions of ions: The deeper red, the higher permeability. Mes-NiNc packing (Figure 3) provides a more significant permeation probability than Ph-NiNc molecular alignments (Figure 2). We predicted partial occupation with the ions in the Ph-NiNc electrode based on the simulations, where the occupation probably happened only on the surface. On the other hand, Mes-NiNc packing showed larger permeable spaces for electrolyte ions, whose occupation would arise smoothly, and full occupation completed.

Authentic morphology distinctions of the solid-state surfaces of Mes-NiNc and Ph-NiNc were then attempted to be observed using an electron microscope. Figure S1 shows SEM images of those electrode materials. Ph-NiNc showed thick and tangled padding, whereas Mes-NiNc exposed clear alignments of fairly thin and smoothly expanded layers. Furthermore, EDX patterns substantially exposed the presence of corresponding elements. Speedily responsible nickel elements precisely reflected their locations rather than nitrogen elements, which verified their strong metal-chelation circumstance (Figure 4).

As supporting our expectation, excellent charge-discharge performances of sodium-organic batteries have been awarded

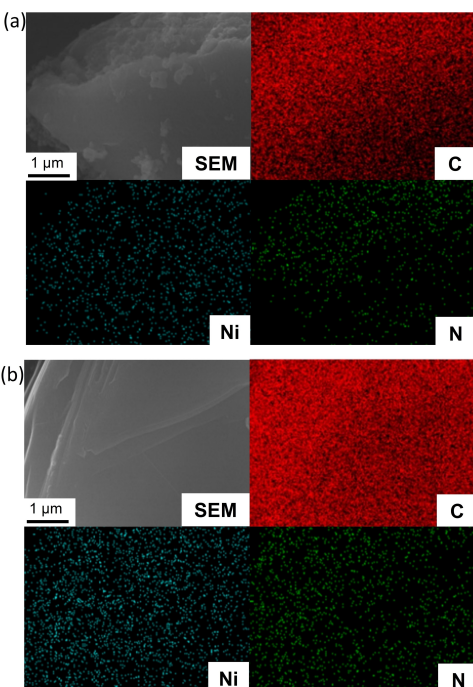


Figure 4. SEM images and EDX patterns: (a) Ph-NiNc and (b) Mes-NiNc.

by implementing Mes-NiNC active electrode in 50% Na[FSA]-[C₂C₁im][FSA] ionic liquid electrolyte. First, the durability of the organic electrode materials in sodium-organic batteries was enhanced significantly using the ionic liquid electrolyte, excluding the dissolution obstacle of electrode materials. Furthermore, the Na-NiNC cell with Mes-NiNC performed comparably larger charge/discharge capacities than the Na-NiNC cell with Ph-NiNC (Figure 5). Theoretically, both Mes- and Ph-NiNC will have a four-electron redox conversion reaction based on two FSA⁻ and two Na⁺. The Mes-NiNC utilizes four electrons, but the Ph-NiNC seems to be only two electrons are involved in the charge/discharge test in Figure 5 due to the packing pattern difference resulted in kinetic limitation for cation-anion insertion/desertion processes. The relatively small capacities of the Ph-NiNC electrode sodium-organic battery were comprehended with the partial dual-ion insertion/desertion happening only on the surface area due to the knotted molecular alignment. Besides, the composition of the positive electrodes has been unified with 70%, 25%, and 5% for NiNC, CB, and PVDF.

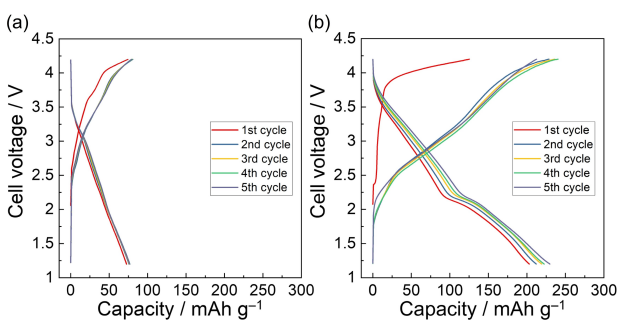


Figure 5. Charge/discharge performances of Na-NiNC cell in 50 mol% Na-[FSA]-[C₂C₁im][FSA] electrolyte: (a) Ph-NiNC and (b) Mes-NiNC. The composition of the positive electrodes is NiNC:CB:PVDF = 70:25:5 wt% and the cut-off voltage is 1.2–4.2 V with the current density of 200 mA g⁻¹.

X-ray diffraction patterns of the NiNC electrodes and NiNC powders were determined to verify the consistency between NiNC electrodes and NiNC powders (Figure S2). The diffractions afforded moderately reliable patterns, indicating the preparation of the electrode did not destroy the molecular packing patterns of NiNC.

Once the consistency between the powder and electrode XRD patterns of Mes-NiNC was established, an in-situ XRD experiment was conducted with a Na-NiNC battery prepared in the same procedure (Figures 6 and S2). The diffractions at 12.6, 15.5, and 18.0° are indexed as 020, 111, and 12-1, respectively. As the patterns represent the highest and the lowest voltages (4.3 and 1.5 V) in a given potential window, those sequences disappeared in accord with anions and cations insertion. However, the middle of the window (2.5 V) showed those diffractions supporting the anions and cations desertions to the correlated positions, consistent with our previous electrochemical results using three-electrode cells.^[4c]

The triple point of the lattice planes was projected upon the crystal lattices based on the lattice planes that were observed from the in-situ XRD experiment. Figure 5(a) presents the selected 2D contour plot of the in-situ XRD patterns. Also, the three *hkl* planes (020), (111), and (12-1) were projected with different orientations focusing on the crystalline packing of Mes-NiNC (Figures 6b-d).

The cavities have been estimated from the Mes-NiNC packing diagram, as represented with the yellow and green spheres in Figure 7. The highest population of the cavity spheres were allocated between two Mes-NiNC closest molecules, substantially matched with the triple point deduced with the three *hkl* planes exposing significant XRD appearance and disappearance.

Computation outcomes substantially supported the insertion and desertion mobilities of dual-ion through Mes-NiNC molecular alignments. The respective ion pairs of [NiNC]^{•-}/Na⁺ (Figure 8) and [NiNC]^{•+}/[FSA]⁻ (Figure 9) occupied reasonably

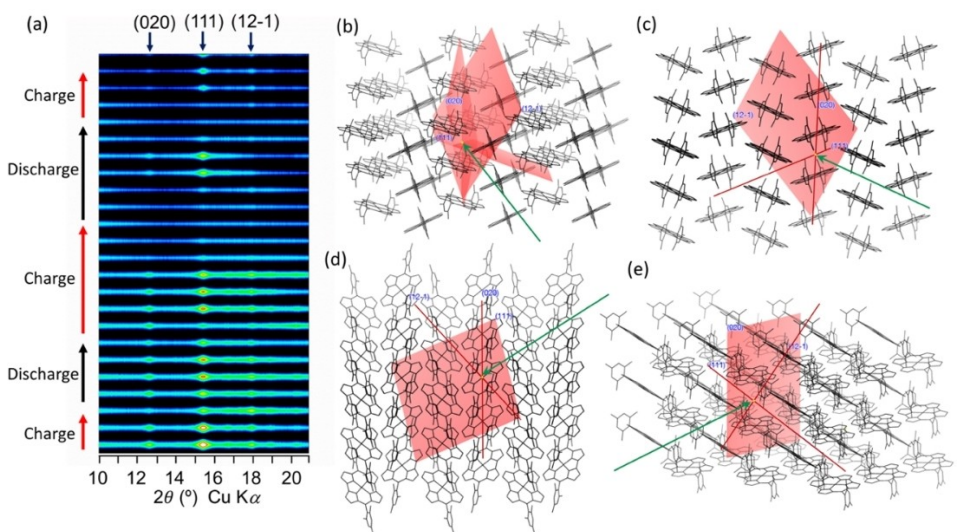


Figure 6. The selected 2D contour plot of in-situ XRD patterns and display of three *hkl* planes, (020), (111), and (12-1) in the crystalline packing of mes-NiNC: (a) The in-situ XRD patterns, (b) 3D view of the three *hkl* planes, and objective views for the selected Miller index planes, (c) (1,2,-1), (d) (1,1,1), and (e) (0,2,0).

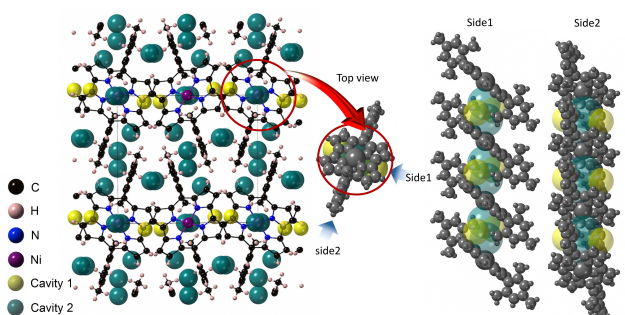


Figure 7. Display of cavities: radii of cavities are estimated with 1.81 Å for the cavity 1 and 2.08~2.24 Å for the cavity 2 of Mes-NiNc.^[9]

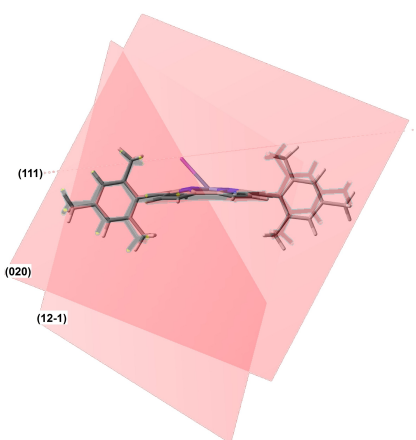


Figure 8. Comparison between a DFT calculated pair of $[\text{NiNc}]^{\bullet-}$ and Na^+ and the triple-point in packing diagram based of in-situ XRD results, an expected position of ion insertion to Mes-NiNc.

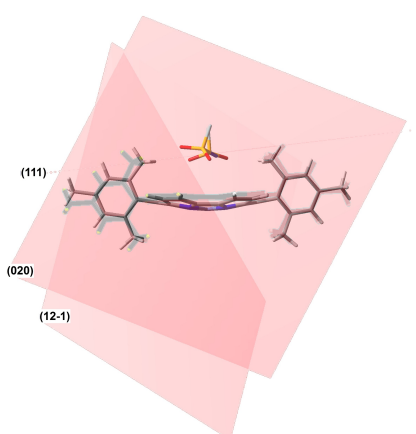


Figure 9. Comparison perspectives of an ionic pair, $[\text{NiNc}]^{\bullet+}$ and $[\text{FSA}]^{\bullet-}$: overlapped view of optimized outcome and the feasible triple-point in packing diagram of Mes-NiNc.

the prospective cavities obtained from Figure 7. The NiNc plane flat initially suspended the attraction and repulsion behaviors of the distinct NiNc ion radical conformations with cation and anion in accord with the redox reactions. NiNc molecules were converted into $[\text{NiNc}]^{\bullet+}$ through the charging process, whose oxidation implemented insertion of anionic FSA. Antiaromatic

nature gives rise to unstable π -electron orbital-energy configuration with an open-shell triplet diradical ground state. It was demonstrated that π -electron delocalization is weakened to degenerate two SOMO-energy levels of antiaromatic molecules and avoid the unstable diradical configuration. Consequently, significant bond length alternations called Jahn-Teller distortion with closed-shell π -electron orbital configurations and narrow HOMO-LUMO gaps can be the characteristics of antiaromatic molecules.^[10] The reduction of antiaromatic molecules probably destabilizes the conformation by adding an electron to the reformatted antiaromatic molecular system. The deformation of the NiNc plane could be resulted from the attraction toward the electron-deficient cationic sodium to reduce the increased electron density by earning an electron (Figure 8). On the other hand, oxidation of antiaromatic molecules probably enhanced the stability by losing an electron. The deformation of the NiNc plane could result from the repulsion against the electron-dense anionic molecule (Figure 9).

Norcorrole shifts its Raman frequencies with the distortion moment as has been reported.^[11] Similar distortion could occur in the respective electrolyte during the production of NiNc electrode: Entire vibration frequencies of the electrode (Figure 10) and the dom-NiNc frequencies early reported were identical. An improved planar, C_{2h} structure was estimated during charge and discharge processes, where the NiNc molecules were transformed into dianionic or dicationic states. Significantly, discharge furnished the reflected Raman frequencies of the initial NiNc powder. Also, the charging process provided a sum of Raman frequencies for two conformations, dom and planar NiNc molecules. $[\text{NiNc}]^{\bullet-}$ and $[\text{NiNc}]^{\bullet+}$ were verified to have dom conformations with structure optimization. However, ultimately charged and discharged states, $[\text{NiNc}]^{\bullet+}$ and $[\text{NiNc}]^{\bullet-}$, comprehended to take flat conformations based on the identical Raman frequencies with the NiNc powder. Figure 7 showed large cavities (2.08–2.24 Å size) positioned above and below the NiNc plane having slipped from the center to the opposite direction for each cavity. The resisted positions for ions induced the planarity of the NiNc molecule reflected in the Raman spectra.

The Na-Mes-NiNc cell precisely performed the charge and discharge processes in a potential window of 1.2–4.2 V with high current densities (Figures 11 and S4). Figure 11 shows a

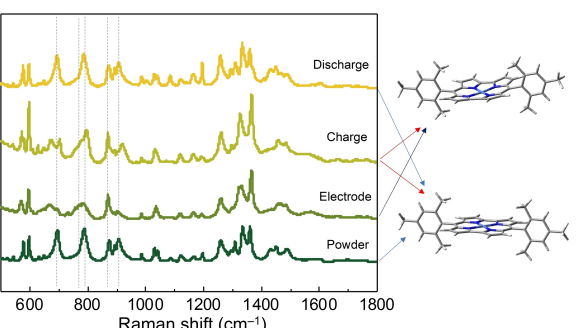


Figure 10. Ex-situ Raman spectra of Na-Mes-NiNc battery.

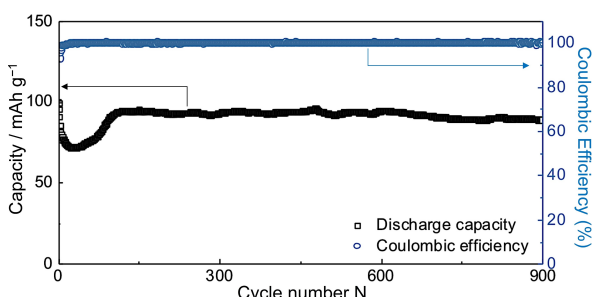


Figure 11. Discharge capacity and efficiency plots of 900 cyclic battery performances of a Na-Mes-NiNc battery: Composition of positive electrode = NiNc:CB:PVDF = 70:25:5 wt %, Cut-off voltages = 1.2–4.2 V, and current density = 2 Ag⁻¹.

set of plots of 900 cyclic charge and discharge performances with an average Coulombic efficiency of 99.8% for 900 cycles. Further electrochemical performance differences in the Na-Mes-NiNc and Na-Ph-NiNc cells are demonstrated with cyclic voltammetry (CV)s measurement (Figure S5).

3. Conclusions

Antiaromatic conformations of NiNc molecules accompanied with Na-organic secondary batteries exhibit sizable charge and discharge performance. Both Na-NiNc batteries prepared with Ph-NiNc and Mes-NiNc electrode materials produced significant charge-discharge processes. Furthermore, we obtained improved battery capacity with the Mes-NiNc electrode. Computational calculations revealed that the vacant space in the molecular packings of Ph-NiNc is less than that of Mes-NiNc. The appropriate hollow spheres in Mes-NiNc molecular alignments were deliberated to amplify the kinetic quantity of the dual-ion, where healthy redox processes with high discharge capacity and Columbic efficiency were accomplished. Furthermore, the determination for the ion pairs, [Mes-NiNc]^{•-}/Na⁺ and [Mes-NiNc]^{•+}/[FSA]⁻, distributed in charging and discharging, were comprehended through optimization, whose orientations and conformations were in good agreement with the in-situ XRD and ex-situ Raman projections.

Experimental Section

Preparation of Ph-NiNc and Mes-NiNc

Ph-NiNc^[6c] and Mes-NiNc^[6a] were prepared following the literature methods from *bis*(2,10-dibromodipyrin)-nickel complexes having meso-phenyl and meso-mesityl, respectively.

Electrochemical measurement

The electrochemical properties were measured in a 2032 type coin cell at 25 °C in the thermostatic chamber SU-242 (ESPEC) using an HJ1001SD8 charge-discharge test device (Hokuto Denko). A current density of 200 mA g⁻¹ and 2 Ag⁻¹ were applied to the charge/discharge, and cycle tests, respectively, with the cut-off voltages of

1.2–4.2 V. CV measurements were with a Bio-Logic VSP potentiostat. Sodium metal (Sigma-Aldrich Chemistry, 99.95% purity) was cut into a disk and fixed on an Al plate current collector as the negative electrode. The positive electrode was prepared by mixing the active material, CB, and PVDF (70:25:5 wt %) and pasting it onto Al foil. A glass microfiber separator (Whatman GF/A) was impregnated in 50 mol % Na[FSA]-[C₂C₁im][FSA] electrolyte.

In-situ XRD experiment

The electrochemical cell for in-situ XRD measurement was prepared in a 2032 type coin cell with a hole on the top case. In-situ XRD measurements were performed using an air-tight cell with a Kapton® window and a temperature controller (Rigaku). The diffraction patterns were recorded at a scan rate of 2° s⁻¹ at 298 K under vacuum. The electrochemical measurements were controlled with an HZ7000 (Hokuto Denko). The cell was continuously charged and discharged at 50 mA g⁻¹ during XRD measurements. Cut-off voltages were fixed at 1.5 V and 4.3 V as the lower and upper limits, respectively.

DFT calculation of ionic pairs

All calculations were afforded with the Gaussian 09 program. The initial geometry of Mes-NiNc was transported from crystallographic data^[6a,c] and optimized. The single reduction and oxidation states, [NiNc]^{•-} and [NiNc]^{•+}, were then calculated with corresponding spin states in the basis set. Finally, counter sodium cation and FSA anion were applied into the redox states to optimize the position. The geometry optimizations were performed with Becke's three-parameter hydride exchange function and the Lee-Yang-Parr correlation functional (B3LYP/Gen).^[12]

Acknowledgements

J.-Y. Shin acknowledges the G30 program foundation of Nagoya University for the financial support and Graduate School of Engineering, Nagoya University for the instrumental support.

Conflict of Interest

The authors declare no conflict of interest.

Keywords: dual-ion battery · durable organic electrode · permeability of organic electrode · sodium organic battery

- [1] a) S. Komaba, W. Murata, T. Ishikawa, N. Yabuuchi, T. Ozeki, T. Nakayama, A. Ogata, K. Gotoh, K. Fujiwara, *Adv. Funct. Mater.* **2011**, *21*, 3859–3867; b) M. Sheng, F. Zhang, B. Ji, X. Tong, Y. Tang, *Adv. Energy Mater.* **2017**, *7*, 1601963; c) B. Park, S. M. Oh, Y. K. Jo, S.-J. Hwang, *Mater. Lett.* **2016**, *178*, 79–82; d) M. Kim, H. M. Hwang, G. H. Park, H. Lee, *FlatChem* **2017**, *6*, 48–76; e) Y. Lee, S. M. Oh, B. Park, B. U. Ye, N.-S. Lee, J. M. Baik, S.-J. Hwang, M. H. Kim, *CrystEngComm* **2017**, *19*, 5028–5037; f) S. M. Oh, I. Y. Kim, S. B. Patil, B. Park, J. M. Lee, K. Adpakpang, S. A. Chae, O. H. Han, S.-J. Hwang, *ACS Appl. Mater. Interfaces* **2017**, *9*, 2249–2260; g) S. Y. Lim, J. H. Lee, S. Kim, J. Shin, W. Choi, K. Y. Chung, D. S. Jung, J. W. Choi, *ACS Energy Lett.* **2017**, *2*, 998–1004; h) L. Wang, C. Wang, N. Zhang, F. Li, F. Cheng, J. Chen, *ACS Energy Lett.* **2017**, *2*, 256–262; i) B. Park, S. M. Oh, Y. K. Jo, S.-J. Hwang, *Mater. Lett.* **2016**, *178*, 79–82; j) B. Park, S. M. Oh, X. Jin, K. Adpakpang, N.-S. Lee, S.-J. Hwang,

- Chem. Eur. J.* **2017**, *23*, 6544–6551; k) W. Wang, W. Li, S. Wang, Z. Miao, H. K. Liu, S. Chou, *J. Mater. Chem. A* **2018**, *6*, 6183–6205; l) W. Cha, I. Y. Kim, J. M. Lee, S. Kim, K. Ramadass, K. Gopalakrishnan, S. Premkumar, S. Umapathy, A. Vinu, *ACS Appl. Mater. Interfaces* **2019**, *11*, 27192–27199; m) H. Wan, W. Weng, F. Han, L. Cai, C. Wang, X. Yao, *Nano Today* **2020**, *33*, 100860; n) L. Yang, P. Wang, S. Zhang, Y. Wang, L. Zang, H. Zhu, J. Yin, H. Y. Yang, *J. Mater. Chem. A* **2020**, *8*, 22791–22801; o) J. M. Lee, G. Singh, W. Cha, S. Kim, J. Yi, S.-J. Hwang, A. Vinu, *ACS Energy Lett.* **2020**, *5*, 1939–1966.
- [2] a) N. Yabuuchi, K. Kubota, M. Dahbi, S. Komaba, *Chem. Rev.* **2014**, *114*, 11636–11682; b) J.-Y. Hwang, S.-T. Myung, Y.-K. Sun, *Chem. Soc. Rev.* **2017**, *46*, 3529–3614; c) J.-J. Kim, K. Yoon, I. Park, K. Kang, *Small Methods* **2017**, *1*, 1700219.; d) E. A. Wu, S. Banerjee, H. Tang, P. M. Richardson, J.-M. Doux, J. Qi, Z. Zhu, A. Grenier, Y. Li, E. Zhao, G. Deysher, E. Sebti, H. Nguyen, R. Stephens, G. Verbist, K. W. Chapman, R. J. Clément, A. Banerjee, Y. S. Meng, S. Ping Ong, *Nat. Commun.* **2021**, *12*, 1256.
- [3] a) M. Armand, J.-M. Tarascon, *Nature* **2008**, *451*, 652–657; b) S. Muench, A. Wild, C. Friebel, B. Häupler, T. Janoschka, U. S. Schubert, *Chem. Rev.* **2016**, *116*, 9438–9484; c) C. Liedel, *ChemSusChem* **2020**, *13*, 2110–2141; d) M. Miroshnikov, K. Mahankali, N. K. Thangavel, S. Satapathy, L. M. R. Arava, P. M. Ajayan, G. John, *ChemSusChem* **2020**, *13*, 2186–2204; e) S. Lv, J. Yuan, Z. Chen, P. Gao, H. Shu, X. Yang, E. Liu, S. Tan, M. Ruben, Z. Zhao-Karger, M. Fichtner, *ChemSusChem* **2020**, *13*, 2286–2294; f) Q. Li, H. Wang, H.-g. Wang, Z. Si, C. Li, J. Bai, *ChemSusChem* **2020**, *13*, 2449–2456; g) J. Yang, H. Su, Z. Wang, P. Sun, Y. Xu, *ChemSusChem* **2020**, *13*, 2436–2442; h) N. Delaporte, G. Lajoie, S. Collin-Martin, K. Zaghib, *Sci. Rep.* **2020**, *10*, 3812; i) B. Esser, F. Dolhem, M. Becuwe, P. Poizot, A. Vlad, D. Brandell, *J. Power Sources* **2021**, *482*, 228814.
- [4] a) J.-Y. Shin, T. Yamada, H. Yoshikawa, K. Awaga, H. Shinokubo, *Angew. Chem.* **2014**, *126*, 3160–3065; *Angew. Chem. Int. Ed.* **2014**, *53*, 3096–3101; b) S. Fujii, S. Margués-González, J.-Y. Shin, H. Shinokubo, T. Masuda, T. Nishino, N. P. Arasu, H. Vázquez, M. Kiguchi, *Nat. Commun.* **2017**, *8*, 15984; c) J. Hwang, R. Hagiwara, H. Shinokubo, J.-Y. Shin, *Mater. Adv.* **2021**, *2*, 2263–2266.
- [5] S. Bai, B. Kim, C. Kim, O. Tamwattana, H. Park, J. Kim, D. Lee, K. Kang, *Nat. Nanotechnol.* **2021**, *16*, 77–84.
- [6] a) T. Ito, Y. Hayashi, S. Shimizu, J.-Y. Shin, N. Kobayashi, H. Shinokubo, *Angew. Chem.* **2012**, *124*, 8670–8673; *Angew. Chem. Int. Ed.* **2012**, *51*, 8542–8545; b) R. Nozawa, K. Yamamoto, J.-Y. Shin, S. Hiroto, H. Shinokubo, *Angew. Chem.* **2015**, *127*, 8574–8577; *Angew. Chem. Int. Ed.* **2015**, *54*, 8454–8457; c) R. Nozawa, H. Tanaka, W.-Y. Cha, Y. Hong, I. Hisaki, S. Shimizu, J.-Y. Shin, T. Kowalczyk, S. Irle, D. Kim, H. Shinokubo, *Nat. Commun.* **2016**, *7*, 13620.
- [7] a) F. P. McCullough, C. A. Levine, R. V. Snelgrove **1989**, US Patent 4830938; b) F. P. McCullough, A. F. Beale, **1989**, US Patent 4865931; c) R. T. Carlin, H. C. Delong, J. Fuller, P. C. Trulove, *J. Electrochem. Soc.* **1994**, *141*, L73; d) M. Sheng, F. Zhang, B. Ji, X. Tong, Y. Tang, *Adv. Energy Mater.* **2017**, *7*, 1601963.
- [8] K. Matsumoto, J. Hwang, S. Kaushik, C.-Y. Chen, R. Hagiwara, *Energy Environ. Sci.* **2019**, *12*, 3247–3287.
- [9] Cavity plots were done with the CrystalMater X software.
- [10] H. J. Wörner, F. Merkt, *J. Chem. Phys.* **2007**, *127*, 034303.
- [11] a) J.-Y. Shin, *J. Porphyrins Phthalocyanines* **2020**, *24*, 191–199.
- [12] a) A. D. Becke, *Phys. Rev. A* **1988**, *38*, 3098; b) C. Lee, W. Yang, R. G. Parr, *Phys. Rev. B* **1988**, *37*, 785.

Manuscript received: August 3, 2021

Accepted manuscript online: August 9, 2021

Version of record online: August 27, 2021